Title

Establishing structure-sensitivity of ceria reducibility: real-time observations of surface-hydrogen interactions

Journal

Journal of Materials Chemistry A, 8(11)

ISSN

2050-7488

Authors

Duchoň, Tomáš
Hackl, Johanna
Mueller, David N
et al.

Publication Date

2020-03-17

DOI

10.1039/c9ta11784a

Peer reviewed

ARTICLE

Establishing Structure–Sensitivity of Ceria Reducibility: Real-Time Observations of Surface–Hydrogen Interactions

Received 00th January 20xx,
Accepted 00th January 20xx

DOI: 10.1039/x0xx00000x

Tomáš Duchoň,*[ab] Johanna Hackl,[a] David N. Mueller,*[a] Jolla Kullgren,[c] Dou Du,[c] Sanjaya D. Senanayake,[d] Caroline Mouls,[e] Daniel M. Gottlob,[a] Muhammad I. Khan,[a] Stefan Cramm,[a] Kateřina Veltruská,[b] Vladimír Matolín,[b] Slavomír Nemšák*[af] and Claus M. Schneider[ag]

The first layer of atoms on an oxide catalyst provides the first sites for adsorption of reactants and the last sites before products or oxygen are desorbed. We employ a unique combination of morphological, structural, and chemical analyses of a model ceria catalyst with different surface terminations under ambience of H_2 to unequivocally establish the effect of the last layer of atoms on surface reduction. (111) and (100) terminated epitaxial islands of ceria are simultaneously studied in situ allowing for a direct investigation of the structure–reducibility relationship under identical conditions. Kinetic rate constants of Ce^{4+} to Ce^{3+} transformation and equilibrium concentrations are extracted for both surface terminations. Unlike the kinetic rate constants, which are practically the same for both types of islands, more pronounced oxygen release, and overall higher reducibility were observed for (100) islands compared to (111) ones. The findings are in agreement with coordination-limited oxygen vacancy formation energies calculated by density functional theory. The results point out the important aspect of surface terminations in redox processes, with particular impact on catalytic reactions for variety of catalysts.

1. Introduction

Catalytic reactions are often classified as structure-sensitive or insensitive, identifying the importance of first layer atomic arrangements to influence reactivity, and establishing the basis for numerous surface science studies.[1,2] The ability to tune catalytic chemistry by altering the surface structure constitutes an important way to take control of reactions. Catalytic conversion can accompany the loss of oxygen from oxide surfaces, typically invoking mechanistic interpretations such as the Mars and Van Krevelen (MvK) type mechanisms. In such cases involving oxidation or reduction of reactants, the role of the catalyst surface is complex, not only providing electrons to facilitate rearrangements of bonds to form the targeted compound, but also having the capability for storing and releasing oxygen, serving as a reductant or oxidant respectively in the catalytic cycle.

Ceria is an ideal reducible oxide prototype benchmark that is often exploited as a redox active catalyst that can impact metal–support interactions, and store or release oxygen to the reaction. Structure sensitivity has been established in some catalytic chemistry,[3] but typically in the presence of a metal. We pose a simpler question regarding the influence of the first layer atomic arrangement in governing the efficacy of H_2 reaction and subsequent removal of oxygen through a reduction of the surface. While interaction of protons with ceria is a rather elementary reaction, its surprising complexity has been recently revealed via contradictory evidence for hydride and hydroxide formation, respectively.[4,5]

We address the question within the structure–activity relationship (SAR) framework, the prevailing concept at the forefront of rational designs and functionalization of materials.[6] An elementary subset of SAR involves facet-dependent properties and processes that allow for straightforward coupling of function to structure, providing convenient means to tailor performance in various applications.[7–9] This has been utilized with great success in the field of heterogeneous catalysis.[10–12] The facet-dependence is typically explored via isolated model systems that facilitate access to a singular structural feature[6]—most commonly a low-index surface plane. While the achievements of the isolated model system approach should not be understated, a considerable limitation of the method lies in the obstacles it imposes on the separation of equilibrium and non-equilibrium thermodynamics. Specifically, such separation necessitates unrealistic precision in the control of thermodynamic variables—i.e., the concentration of participating species and temperature. Consequently, studies of

[a] Peter-Grünberg-Institut 6, Forschungszentrum Jülich GmbH, 52425 Jülich, Germany
[b] Department of Surface and Plasma Science, Faculty of Mathematics and Physics, Charles University, 18000 Prague, Czech Republic
[c] Department of Chemistry–Ångström Laboratory, Uppsala University, Box 538, S-751 21 Uppsala, Sweden
[d] Department of Chemistry, Brookhaven National Laboratory, Upton, New York 11973, USA
[e] Laboratório Nacional de Luz Síncrotron, 13083 Campinas - SP, Brazil
[f] Advanced Light Source, Lawrence Berkeley National Laboratory, Berkeley, CA, USA
[g] Department of Physics, University of California, Davis, CA, USA
† Electronic Supplementary Information (ESI) available. See
DOI: 10.1039/x0xx00000x

facet-dependent dynamics in heterogeneous catalysis are limited to chemical, rather than physical, investigations[13,14] or non-trivial techniques.[15]

The importance of the limitation mentioned above is emphasized in the case of ceria, and reducible oxides in general.[16,17] One of the parameters governing the chemistry of reducible oxides is the oxygen vacancy formation energy.[18,19] Upon forcing the system away from equilibrium by an external stimulus, i.e. supplying an oxidant or reductant, egalization of the (oxygen) chemical potentials of solid and gas as governed by the vacancy formation energy in the former is achieved by a cascade of electron and ion transfers across the solid–gas interface, the microkinetic progression of which is guided by the activation barriers of these transfer processes. Any reduction-oxidation processes are therefore necessarily contingent upon both oxygen vacancy formation energetics and the microkinetic pathway in a convoluted manner. The heterogeneous nature of the microkinetic pathway necessitates the involvement of adsorption sites, a factor strongly dependent on the surface orientation.[20]

In this work, we present a significant improvement of the model system approach that allows for direct real-time comparison of facet-dependent properties of reducible oxides under identical thermodynamic conditions, effectively bypassing the required high precision in the control of thermodynamic variables. Utilizing recent advances in the heteroepitaxial growth of oxides on metals,[21] we prepare islands of ceria,[22] a prototypical reducible oxide, exposing (111) and (100) surfaces side by side on Cu(111). Taking advantage of the imaging capabilities of low-energy electron microscopy (LEEM) and X-ray photoemission electron microscopy (X-PEEM), which were previously demonstrated in the case of the ceria (111) surface,[23–25] we follow the structural and chemical properties of the (111) and (100) surface planes of ceria under a reducing H_2 atmosphere simultaneously and in situ on the timescale of the reduction process. The direct comparison allows us to show that the difference in the facility of H_2 oxidation of the two surface planes of ceria is not determined by the kinetic rate constants of the reduction reaction, but rather by the equilibrium concentration of oxygen vacancies. This means that attributes of either surface orientation are inconsequential for the rate-determining step of the reaction. Notably, no evidence of oxidation via hydride formation during the interaction with H_2 was observed for either surface. These insights could not be provided by the isolated model system approach to date and, most importantly, the presented methodology is easily generalized to other reducible oxides.

1. Experimental

2.1 X-ray photoemission electron microscopy

All experiments were carried out with the FE-LEEM P90 AC instrument commercialized by SPECS and installed as a permanent end-station at the soft X-ray undulator beamline UE56/1-SGM at the synchrotron facility BESSY II in Berlin. This instrument enables the use of LEEM, X-PEEM, UV-PEEM, micro low-energy electron diffraction (μ-LEED), and micro X-ray absorption spectroscopy (μ-XAS) as combined methods in situ. The background pressure of the apparatus was 5×10^{-10} mbar.

Ceria islands were grown on a Cu(111) single crystal (MaTeck, cut with 0.1° accuracy) via reactive physical vapor deposition. Prior to the deposition, the Cu(111) substrate was cleaned by several cycles of Ar^+ sputtering (1.5 kV) and annealing at 870 K in UHV and 5×10^{-7} mbar of O_2 (Linde, 99.998%). The mean terrace width of the prepared substrate is of the order of tens to hundreds of nm. Cerium (GoodFellow, 99.9%) was evaporated in 5×10^{-7} mbar of O_2 from a Focus EFM 3T evaporator using a tungsten crucible with the substrate kept at the temperature of 720 K. The growth parameters were optimized based on previous works, which demonstrated that it is possible to prepare both (111) and (100) oriented ceria islands on Ru(0001) and Cu(111).[26–28] Details of the ceria island growth are shown in the Supplementary Information (SI), including LEEM images of various stages of the sample preparation (Figure S1).

The thickness of the prepared ceria islands has been determined from the attenuation of Cu L_3 XAS edge (Figure S2). It should be noted, though, that the total electron yield (TEY) signal employed in this study includes secondary electrons, rendering the information depth and use of inelastic mean free path (IMFP) of electrons ambiguous. Frazer et al. experimentally determined a characteristic $1/e$ length (a thickness of material that attenuates TEY signal by a factor of $1/e$) of 21 Å for TEY measurements at the Cu L_3 peak through an overlayer of Cr.[29] Cr and ceria have very similar densities of 7.190 g/cm^3 and 7.215 g/cm^3. Moreover, the TPP2M method commonly used for IMFP calculation for inelastically scattered electrons, which takes into account also band gap and character of valence electrons, gives practically the same values for Cr and ceria.[30] Therefore, we assume that the $1/e$ value obtained for TEY signal of Cu L-edge for Cr is also valid for ceria. Using this characteristic attenuation length, the ceria island thickness for both the (111) and (100) case are determined to be ca. 9 Å, i.e. ~ 3 monolayers (ML = O–Ce–O trilayer), with a ML thickness of 3.12 Å for the (111) and 2.71 Å for the (100) orientation.

The stoichiometry of the ceria islands was determined from the Ce M_5 XAS signal via comparison to reference Ce^{4+} and Ce^{3+} spectra (Figure 2) by the least square method. The Ce^{4+} and Ce^{3+} reference spectra were obtained from the as prepared islands kept in O_2 pressure of 5×10^{-7} mbar and from islands reduced to the bixbyite c-Ce_2O_3 via Ce–ceria interfacial interaction, respectively.[21] The reference spectra match previously published results measured elsewhere.[23] Exponential attenuation of the signal passing through the overlayer was then used to calculate the actual stoichiometry of the 3 ML ceria islands. Two assumptions in the analysis were: 1. All of the oxygen vacancies and, consequently, the Ce3+ ions are present in the topmost 3 Å of the islands, as predicted by DFT (see below). 2. Signal attenuation length for the Ce M_5 edge was estimated to be 20 Å, in accordance with the previously discussed thickness analysis using the Cu L_3 edge. We note that if the first assumption is not used and the Ce_{3+} ions are instead assumed to be homogeneously distributed in the film a slightly

higher reduction is arrived at (i.e., after 23 h of H_2 exposure: $CeO_{1.87}$ instead of $CeO_{1.88}$ and $CeO_{1.81}$ instead of $CeO_{1.83}$ for the (111) and (100) terminated islands, respectively), but the trends are consistent.

2.2 Computational details

All simulations presented here are based on density functional theory (DFT) in the implementation with plane waves and pseudopotentials using the Hybrid density functional proposed by Heyd-Scuseria-Ernzerhof (HSE06).[31,32] The electronic wavefunctions were expanded in a plane-wave basis set with a kinetic energy cut-off of 408 eV. The core−valence interactions were modeled with pseudopotentials generated within the Projector Augmented Wave (PAW) scheme proposed by Blöchl.[33] In the calculations, we explicitly treated 6 and 12 electrons for each oxygen and cerium atom, respectively. All calculations were made using the Vienna Ab-initio Simulation Package (VASP).[34–36]

3. Results and discussion

A schematic of the experimental layout is shown in Figure 1(a). Ceria (111) and (100) islands are grown simultaneously, and both populations can be observed within the selected field-of-view. Figure 1(b) shows the as prepared ceria islands imaged by LEEM. The confirmation of two different surface terminations of the islands was performed by µ-LEED, showing a hexagonal pattern for the (111) surface and a square pattern with a (√2×√2)R45° reconstruction for the (100) surface (see Figures 1(c) and (d)). The reconstruction of the (100) surface is expected due to bulk (100) terminations of ceria having a dipole moment perpendicular to the surface.[37] While the actual atomic structure is still under debate, the (√2×√2)R45° reconstruction has been previously observed for ceria (100) islands with a thickness of 3 ML.[38] We note that 1 ML thick islands with a (1×1) reconstruction and 10 ML thick islands with a (2×2) reconstruction have also been reported.[21,39,40]

After the growth, the ceria islands are exposed to a reducing atmosphere of 1.5×10^{-6} mbar of H_2 (Linde, 99.999 %) at 700 K for an extended time (23 h). The reduction of the islands is observed with X-PEEM imaging and µ-XAS at the Ce M_5 edge

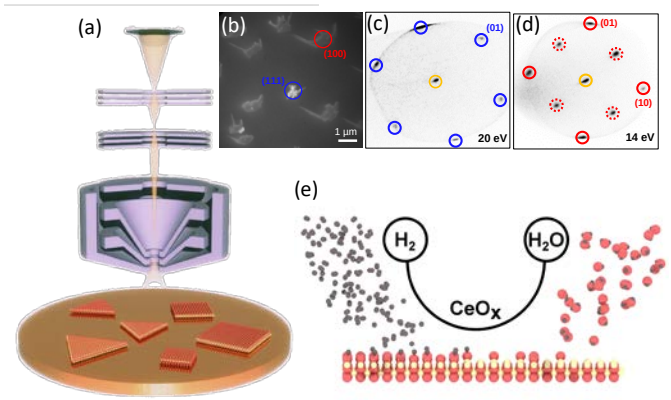

Figure 2. (a) Schematics of the experimental layout. (b) LEEM image of grown ceria islands recorded at 9 eV. (c) and (d) respective µ-LEED patterns for the two ceria island terminations. (e) Schematic of the H_2 oxidation reaction by CeO_2.

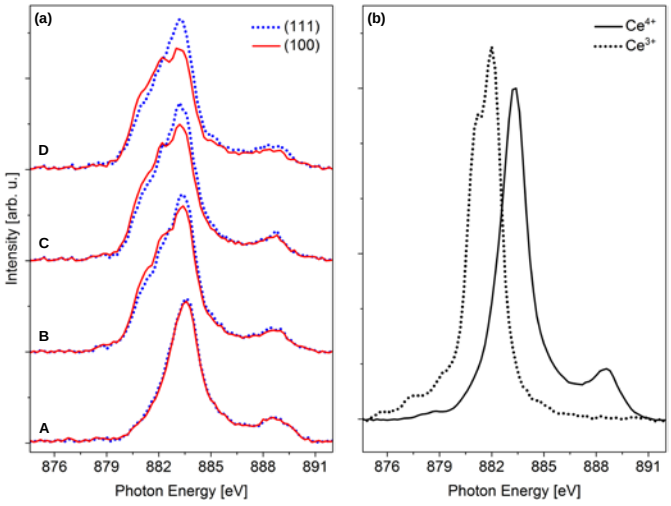

Figure 1. (a) X-ray absorption spectra at the Ce M_5 edge acquired from the ceria (111) and (100) islands marked in Figure 1(b): **A** initial CeO_2 in vacuum at 700 K, **B** after 14.5 h in 1.5×10^{-6} mbar of H_2 at 700K, **C** and **D** after 18.5 and 21.5 h, respectively, (b) Reference spectra for Ce^{3+} and Ce^{4+} used to determine the stoichiometry.[45]

during the reduction at reaction conditions. Successively measured spectra in Figure 2(a) show progressive changes in the spectral shape indicative of evolution of different oxidation states for the (111) and (100) islands marked in Figure 1(b). In the initial state (graph A), both the (111) and the (100) islands are fully oxidized and contain almost exclusively Ce^{4+} ions. The features in trace A are distinctive for Ce^{4+} ions, with the main peak at 883.4 eV and a satellite peak with lower intensity at the higher energy flank, which indicates the hybridization between O 2p and Ce 4f orbitals.[41,42] After several hours of H_2 exposure, the ceria islands reduce gradually to CeO_{2-x}. On the lower energy side of the Ce M_5 white-line peak, two additional peaks appear at 882.0 and 881.2 eV and become more pronounced over time (traces B–D). These additional peaks are distinctive for Ce^{3+} and therefore indicate the reduction of ceria.[43,44] During the reduction process, the spectra obtained from the (100) island (solid red lines) always reveal a higher degree of reduction than the ones belonging to the (111) island (dotted blue lines). In order to determine the oxidation state of the ceria from the Ce M_5 edge spectra, the experimental data is fitted to a linear combination of the Ce^{4+} and Ce^{3+} reference spectra,[45] which were measured separately and are shown in Figure 2(b). After 23 h of H_2 exposure, the observed oxidation states of the (111) and the (100) islands are $CeO_{1.88}$ and $CeO_{1.83}$, which is equivalent to remaining Ce^{4+} contents of 76 % and 66 %, respectively. This difference in reduction can also be seen in the X-PEEM images (Figure S3).

The development of the islands' Ce^{4+} content over time in H_2 is displayed in Figure 3(a). We consistently observed a delay of about 2 h between the start of the H_2 exposure and the start of the reduction process, when repeating this experiment several times. This delay is very likely due to reoxidation of the ceria islands via oxygen spillover from an adlayer on the Cu(111) substrate (the islands were deposited in O_2 ambience). Such an effect has already been observed for ceria grown on an Rh(111) substrate.[24] Consequently, the ceria reduction only becomes visible after the oxygen adlayer on the substrate is depleted.

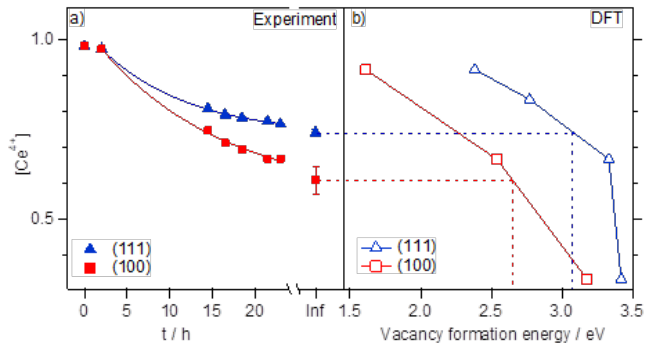

Figure 3. (a) Ce^{4+} content of ceria islands over time in H_2 and fits to the kinetic model (Eq. (3), solid lines) for (111) and (100) islands for delayed reduction with incubation time t_i = 2 h with results in Table 1 and elaboration of how these concentrations are derived from the XAS in the Supplementary information. The values shown for infinity (Inf) are obtained from the fit to the kinetic model. (b) Oxygen vacancy formation energies as a function of Ce^{4+} content calculated using DFT from a 3 ML slab (here shown with reversed axes for better comparison to experiment). Solid lines are guides to the eye; dashed lines indicate the vacancy formation energies calculated for the respective equilibrium conditions.

The reduction of ceria with H_2 progresses via the following equilibrium (written in the Kröger-Vink notation[46]):

$$H_2 + 2Ce_{Ce}^{x} + O_O^{x} \rightleftharpoons 2Ce_{Ce}' + H_2O + V_O^{\bullet\bullet} \qquad (1)$$

It should be noted that the reaction above assumes a complete removal of water from the catalyst, i.e. that in equilibrium no hydroxyls are incorporated into the CeO_2 lattice as shown in Eq. 2

$$H_2 + 2Ce_{Ce}^{x} + 2O_O^{x} \rightleftharpoons 2Ce_{Ce}' + 2OH_O^{\bullet} \qquad (2)$$

Indeed, for relatively high partial pressures of H_2O/H_2 the concentration of oxygen vacancies has been found to be negligible and independent of the effective oxygen chemical potential.[47] However, for the pressure and temperature regime of this experiment, a limited coverage of water has been found,[48] which makes Eq. 1 more plausible than Eq. 2 and which is also in accordance with the findings in this work as explained later.

Qualitatively speaking, the reduction process leads to a lower Ce^{4+} content in the (100) islands than in the (111) islands at all times. The concentration of Ce^{4+} ions in both cases decreases towards an equilibrium, which is far from the total reduction of the whole islands into Ce_2O_3. The complete reduction to Ce_2O_3 would also be accompanied by a phase transformation into a bixbyite structure and significant changes in the μ-LEED patterns and reflectivity of the surface in LEEM.[49] The incomplete reduction is also in accordance with the results of Sayle et al., who used molecular dynamics simulations for atomistic models of ceria nanostructures.[50] Their simulations showed that the gradual depletion of oxygen from a ceria nanocatalyst makes it energetically more difficult to extract further oxygen.

With a time-resolved concentration profile and all relevant defect concentrations connected by simple relations, the kinetics of the ceria reduction can be assessed quantitatively for both orientations. The reduction of ceria with H_2 is proposed to take place via a two-step mechanism,[51] the first step being the dissociative adsorption of H_2 to form surface hydroxyls (Eq. 2), involving an electron transfer from the H_2 molecule to the Ce ion, which is consequently reduced from Ce^{4+} to Ce^{3+}. This may be followed by the removal of an H_2O molecule, leaving behind an oxygen vacancy (Eq. 1) or not (Eq. 2). The electron transfer step being rate-limiting,[47] the reduction of ceria can thus be described by first-order kinetics[52] rendering whether water removal actually occurs insignificant for the rate law. The time-dependent concentration of Ce^{4+} $C(t)$ is then given by:

$$C(t) = \left(1 - e^{-k(t-t_i)}\right)(C_\infty - C_0) + C_0 \qquad (3)$$

Here C_0 is the Ce^{4+} content before the beginning of the reduction process, C_∞ is the Ce^{4+} content at the reduced equilibrium state, and k is the chemical rate constant. The introduction of an incubation time t_i is necessary, as explained above. By fitting this model to our data, we are able to extract kinetic (the rate constant k) as well as thermodynamic (the equilibrium concentration of Ce^{4+} C_∞) data as shown in Fig. 3(a). The values of the rate constant k for the reduction kinetics for the (111) and the (100) islands are summarized in Table 1. Both values are remarkably close to the value of 1.5 × 10^{-5} s^{-1} found for polycrystalline samples.[53] The fact that the rate constant virtually does not depend on the surface orientation, considering an order of magnitude difference in oxygen storage capacity of the two surfaces,[14] and is close to the value for an ill-defined surface with a mixture of surface orientations[53] points to the conclusion that the surface exchange rate, at least in the reduction reaction under the thermodynamic conditions present in this work, is independent of the surface orientation and thus follows the same mechanism.

In terms of the thermodynamics, we find a larger deviation for the C_∞ parameter for the different surface orientations, summarized in Table 1. The magnitude of both concentrations lies in the plausible regime of surface concentrations found before.[51,54] The difference in the equilibrium values, however, shows strikingly different reducibility of the (111) and (100) islands.

Approximate comparison of energetics extracted from the experiments between the two orientations gives valuable insights into what the underlying thermodynamics of the difference in reducibilities are. The relation between Gibbs free energies ΔG and equilibrium constants of reaction (1) can be written as:

	(111)	(100)
k [s^{-1}]	(3.02 ± 0.22) × 10^{-5}	(2.44 ± 0.33) × 10^{-5}
C_0 [1]	0.980 ± 0.003	0.980 ± 0.008
C_∞ [1]	0.741 ± 0.009	0.608 ± 0.044

Table 1. Fitting parameters of a kinetic model for (111) and (100) terminated islands.

$$\Delta G = -k_B T \ln(K) \quad (4)$$

The equilibrium constant K of the reaction shown in Eq. (2) is given by the appropriate concentrations as:

$$K = \frac{\mathrm{pH_2O} \cdot [Ce'_{Ce}]^2 \cdot [V_O^{\bullet\bullet}]}{\mathrm{pH_2} \cdot [Ce^x_{Ce}]^2 \cdot [O^x_O]} \quad (5)$$

Assuming charge neutrality of the cation and anion lattices and owing to the simultaneous nature of the experiment keeping the partial pressures identical, the only independent variable between the two orientations are the respective equilibrium Ce^{4+} concentrations C_∞, as $[Ce'_{Ce}] = 1 - [Ce^x_{Ce}]$; $[Ce'_{Ce}] = 2[V_O^{\bullet\bullet}]$ and, consequently, $C_\infty = [Ce^x_{Ce}] = 2[O^x_O]$. Using the set of equations (4) and (5) for the two surface terminations, one can extract the difference of the Gibbs free energies $\Delta G_{111} - \Delta G_{100} = 0.16$ eV. Here again, it is irrelevant whether the reaction follows Eq. (1) or (2), the Gibbs free energy then describing either the hydration or reduction of ceria.

In order to better understand the origin of this difference in reducibility and to make an assessment which of the reactions is more plausible, we turn to density functional theory (DFT). For the case of a complete reduction (Eq. 1), the problem can be essentially reduced to finding the relation between the oxygen vacancy formation energy and the oxygen vacancy coordination (and concentration) at the surface of ceria. Previous studies have already explored this relation for the case of the (111) surface termination.[55] Here, we reproduce the results on a 3 ML thick slab (corresponding to the thickness of the ceria islands in the experiment) for the (111) surface termination and extend the calculations to the (100) surface termination (Figure 3 (b)). Numerical values are shown in Tables S1 and S2 of SI. Several well-established trends are apparent from the calculated oxygen vacancy formation energies on the (111) surface. First, the vacancies favor localization in the sub-surface layer (the bottom oxygen layer of the first O–Ce–O trilayer). Second, the oxygen vacancy formation energy grows monotonously with the oxygen vacancy concentration and reaches a very stable plateau when one-fourth of the oxygen atoms are removed from the subsurface layer. This configuration corresponds to a (2×2) ordering of oxygen vacancies, which has been observed both in previous experimental and theoretical works.[56] Further formation of oxygen vacancies on the (111) surface exhibits a marked increase in energy cost. This can be rationalized by the observation that removal of further oxygen from the sub-surface layer would inevitably lead to the formation of nearest neighbor oxygen vacancies, essentially representing linear clusters. It is worth noting that if the system has enough energy to overcome this barrier, further reduction up to the removal of all the oxygen from the subsurface layer does not impose a markedly increased energy cost. In short, the DFT results from the (111) surface termination tell us that if the system does not have enough energy, the reduction of the (111) surface will stop when it reaches the (2×2) coordinated oxygen vacancies corresponding to the removal of one-fourth of the oxygen from the sub-surface layer. In this configuration, the 3 ML thick ceria slab exhibits a stoichiometry of $CeO_{1.92}$ ($Ce_{48}O_{92}$).

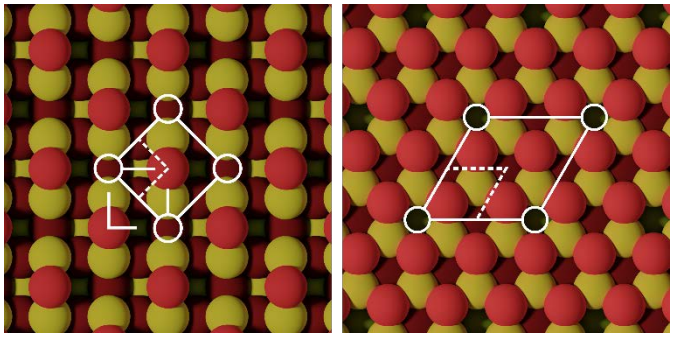

Figure 4. Oxygen vacancy configuration at the equilibrium for (100) termination (left panel) and (111) termination (right panel). Dashed lines show the original, unreconstructed unit cells. The reconstructed unit cells after oxygen removal are outlined by solid lines.

The (100) surface termination exhibits several important differences in terms of the calculated properties of oxygen vacancies. The first variation from the (111) case is in the preferred localization of the oxygen vacancies. Specifically, the oxygen vacancies tend to localize in the surface layer, with the sub-surface position being already close to the bulk oxygen vacancy formation energy. Secondly, the oxygen vacancy formation energy increases linearly with the oxygen vacancy concentration without any marked barrier, as was the case for the (111) surface. Importantly, the geometry of the (100) surface allows removing up to one-half of the oxygen atoms from the surface before formation of nearest neighbor oxygen vacancies sets in. Interestingly, it is at this point where the oxygen vacancy formation energy matches that of the (2×2) coordination of oxygen vacancies on the (111) surface that also represents the point where nearest neighbor oxygen vacancies start to form.

The DFT calculated oxygen vacancy formation energies for both terminations indicate that if the driving force of the reduction is not sufficient to overcome the energy barrier represented by the (2×2) coordinated oxygen vacancies on the (111) surface, only one-fourth of the oxygen can be removed from the (111) surface of ceria, while one half of the oxygen can be removed from the (100) surface, converging the reasons for the different reducibilites to a steric argument: Oxygen vacancies just do not want to be nearest neighbors. Interestingly, the formation enthalpy of water with a value of ~2.4 eV at these experimental conditions is quite close to this threshold. In other terms, the formation of water does not provide enough energy to create vacancies that are the next nearest neighbors. Converting the values to stoichiometry for 3 ML thick islands, we arrive at $CeO_{1.92+/-0.01}$ and $CeO_{1.83+/-0.01}$ for the (111) and (100) surfaces, respectively. The theoretical results are remarkably close to the experimental stoichiometry values (determined from the C_∞ of the first-order kinetic model) of $CeO_{1.87+/-0.02}$ and $CeO_{1.80+/-0.01}$ for the (111) and (100) islands, respectively. Extrapolating the vacancy formation energies obtained from DFT to the experimental values shows that at the equilibrium values the former only differ by 0.5 eV (see Fig. 3). Figure 4 depicts the equilibrium configuration of oxygen vacancies for both (111)

and (100) terminations as obtained from DFT and experimental data.

In accordance with the initial assumption, the surface orientation does have an impact on the reduction behavior of the ceria islands. However, the kinetics of the ceria reduction are almost the same for the (111) and the (100) surface orientations. This might point towards the microkinetic processes being the same for both surface orientations. It is the higher reducibility of the ceria (100) surface, which leads to an easier (and faster in absolute values) reduction of the (100) terminated islands compared to the (111) and shows that the main difference between the two surfaces lies in the thermodynamics. This assertion can be simplified even more, as the DFT shows in accordance with experimental values that there is a quite intuitive geometric limit to the reduction: Having all vacancies accumulated in the surface-most unit cell, the barrier is merely the energetic penalty for two oxygen vacancies being forced to be next nearest neighbors. In conjunction with the kinetics being identical, this limit to the reducibility of the ceria islands supports the idea that a more ready supply of oxygen from the (100) oriented islands increases the activity towards oxidative catalysis.[50] We note, however, that at higher temperatures or utilizing stronger reducing agents the kinetics for the two surfaces might diverge via entropic contributions[57] or oxygen migration pathways.[58]

Conclusions

To summarize, we managed to produce and compare the chemistry of epitaxial ceria (111) and (100) islands on a Cu (111) substrate side by side for the structure sensitivity of H_2 reducibility. Using a combination of LEEM, μ-LEED, X-PEEM, and μ-XAS, we present unique simultaneous chemical, structural, and morphological analysis in real-time of the redox behavior for (111) and (100) CeO_x surfaces under identical driving forces. Both surfaces reduce gradually in H_2 atmosphere at 700 K without any observable hydride formation, and, specifically, no oxidation as previously reported at room temperature.[4] We dynamically observed a more pronounced reduction of the (100) terminated ceria islands compared to the (111) terminated ones, in accordance with DFT calculations performed. Assessing the reduction kinetics for each face revealed that the difference in the catalytic activity of the surface orientations rather lies in the thermodynamics of reduction than the kinetics of the oxygen exchange. Corroborated by DFT calculation this difference can be broken down to an intuitive geometric reason: The repulsion of oxygen vacancies in the surface. This is important consideration for the design principles for more complex oxide catalysts.

Conflicts of interest

There are no conflicts to declare.

Acknowledgements

T.D. acknowledges the support from the Czech Science Foundation (GAČR 15-06759S) and the Grant Agency of Charles University (GAUK 472216). S.D.S. was funded by the US Department of Energy Office of Science and Office of Basic Energy Sciences under Contract No. DE-SC0012704. J.K. would like to acknowledge Åforsk. The simulations were performed on resources provided by the Swedish National Infrastructure for Computing (SNIC) at UPPMAX and NSC.

Notes and references

1 G. A. Somorjai and J. Carrazza, *Ind. Eng. Chem. Fund.*, 1986, **25**, 63−69.
2 M. Boudart, *Adv. Catal.*, 1969, **20**, 153.
3 H. Cordatos, T. Bunluesin, J. Stubenrauch, J. M. Vohs and R. J., *J. Phys. Chem.*, 1996, **100**, 785−789.
4 Z. Li, K. Werner, K. Qian, R. You, A. Płucienik, A. Jia, L. Wu, L. Zhang, H. Pan, H. Kuhlenbeck, S. Shaikhutdinov, S., W. Huang and H.-J. Freund, *Angew. Chem., Int. Ed.*, 2019, **58**, 14686−14693.
5 A. H. Clark, K. A. Beyer, S. Hayama, T. I. Hyde and G. Sankar, *Chem. Mater.*, 2019, **31**, 7744−7751.
6 H.-J. Freund, *Chem.: Eur. J.*, 2010, **16**, 9384–9397.
7 S. Selcuk and A. Selloni, *Nat. Mater.*, 2016, **15**, 1107–1112.
8 S. Y. Leblebici, L. Leppert, Y. Li, S. E. Reyes-Lillo, S. Wickenburg, E. Wong, J. Lee, M. Melli, D. Ziegler, D. K. Angell, D. F. Ogletree, P. D. Ashby, F. M. Toma, J. B. Neaton, I. D. Sharp and A. Weber-Bargioni, *Nat. Energy*, 2016, **1**, 16093.
9 X.-Y. Yu, Q.-Q. Meng, T. Luo, Y. Jia, B. Sun, Q.-X. Li, J.-H. Liu and X.-J. Huang, *Sci. Rep.*, 2013, **3**, 2886.
10 J. Pal and T. Pal, *Nanoscale*, 2015, **7**, 14159–14190.
11 S. Rej, C.-F. Hsia, T.-Y. Chen, F.-C. Lin, J.-S. Huang and M. H. Huang, *Angew. Chem., Int. Ed.*, 2016, **55**, 7222–7226.
12 M. Cao, Z. Tang, Q. Liu, Y. Xu, M. Chen, H. Lin, Y. Li, E. Gross and Q. Zhang, *Nano Lett.*, 2016, **16**, 5298–5302.
13 T. Chen, S. Chen, P. Song, Y. Zhang, H. Su, W. Xu and J. Zeng, *ACS Catal.* 2017, **7**, 2967–2972.
14 G. Vilé, S. Colussi, F. Krumeich, A. Trovarelli and J. Pérez-Ramírez, *Angew. Chem., Int. Ed.*, 2014, **53**, 12069–12072.
15 B. Goris, S. Turner, S. Bals and G. Van Tendeloo, *ACS Nano*, 2014, **8**, 10878–10884.
16 U. Diebold, *Surf. Sci. Rep.* **48**, 53–229 (2003).
17 T. Montini, M. Melchionna, M. Monai and P. Fornasiero, *Chem. Rev.* 2016, **116**, 5987–6041.
18 E. W. McFarland and H. Metiu, *Chem. Rev.* 2013, **113**, 4391–4427.
19 J. Paier, C. Penschke, and J. Sauer, *Chem. Rev.* 2013, **113**, 3949–3985.
20 M. Molinari, S. C. Parker, D. C. Sayle and M. S. Islam, *J. Phys. Chem. C* 2012, **116**, 7073–7082.
21 J. Höcker, T. Duchoň, K. Veltruská, V. Matolín, J. Falta, S. D. Senanayake and J. I. Flege, *J. Phys. Chem. C* 2016, **120**, 4895–4901.
22 D. R. Mullins, *Surf. Sci. Rep.* 2015, **70**, 42–85.
23 J. Höcker, T. O. Menteş, A. Sala, A. Locatelli, T. Schmidt, J. Falta, S. D. Senanayake and J. I. Flege, *Adv. Mater. Interfaces* 2015, **2**, 1500314.
24 D. C. Grinter, C. Muryn, A. Sala, C.-M. Yim, C. L. Pang, T. O. Menteş, A. Locatelli and G. Thornton, *J. Phys. Chem. C* 2016, **120**, 11037–11044.
25 D. C. Grinter, S. D. Senanayake and J. I. Flege, *Appl. Catal. B Environ.* 2016, **197**, 286–298.
26 Y. Pan, N. Nilius, C. Stiehler, H.-J. Freund, J. Goniakowski and C. Noguera, *Adv. Mater. Interfaces* 2014, **1**, 1400404.
27 O. Stetsovych, J. Beran, F. Dvořák, K. Mašek, J. Mysliveček and V. Matolín, *Appl. Surf. Sci.* 2013, **285**, 766–771.

28 J. I. Flege, J. Höcker, B. Kaemena, T. O. Menteş, A. Sala, A. Locatelli, S. Gangopadhyay, J. T. Sadowski, S. D. Senanayake and J. Falta, *Nanoscale* 2016, **8**, 10849–10856.
29 B. H. Frazer, B. Gilbret, B. R. Sonderegger and G. De Stasio, *Surf. Sci.* 2003, **537**, 161–167.
30 S. Tanuma, C. J. Powell and D. R. Penn, *Surf. Interface Anal.* 2003, **35**, 268–275.
31 J. Heyd, G. E. Scuseria and M. Ernzerhof, *J. Chem. Phys.* 2003, **118**, 8207.
32 J. Heyd, G. E. Scuseria and M. Ernzerhof, *J. Chem. Phys.* 2006, **124**, 219906.
33 P. E. Blöchl, *Phys. Rev. B* 1994, **50**, 17953−17979.
34 G. Kresse, J. Hafner, *Phys. Rev. B* 1993, **47**, 558−561.
35 G. Kresse, J. Hafner, *Phys. Rev. B* 1994, **49**, 14251−14269.
36 G. Kresse, J. Furthmüller, *Comput. Mater. Sci.* 1996, **6**, 15−50.
37 C. Noguera, F. Finocchi and J. Goniakowski, *J. Phys. Condens. Matter* 2004, **16**, S2509–S2537.
38 O. Stetsovych, J. Beran, F. Dvořák, K. Mašek, J. Mysliveček and V. Matolín, *Appl. Surf. Sci.* 2013, **285**, 766–771.
39 F. Yang, Y. Choi, S. Agnoli, P. Liu, D. Stacchiola, J. Hrbek and J. A. Rodriguez, *J. Phys. Chem. C* 2011, **115**, 23062–23066.
40 Y. Pan, N. Nilius, C. Stiehler, H.-J. Freund, J. Goniakowski, C. Noguera, *Adv. Mater. Interfaces* 2014, **1**, 1400404.
41 R. C. Karnatak, J.-M. Esteva, H. Dexpert, M. Gasgnier, P. E. Caro and L. Albert, *Phys. Rev. B* 1987, **36**, 1745–1749.
42 T. Duchoň, M. Aulická, E. F. Schwier, H. Iwasawa, C. Zhao, Y. Xu, K. Veltruská, K. Shimada andV. Matolín, *Phys. Rev. B* 2017, **95**, 165124.
43 L. A. Garvie, and P. R. Buseck, *J. Phys. Chem. Solids* 1999, **60**, 1943–1947.
44 S. O. Kucheyev, B. J. Clapsaddle, Y. M. Wang, T. Van Buuren and A. V. Hamza, *Phys. Rev. B* 2007, **76**, 235420.
45 J. Hackl, T. Duchoň, D. M. Gottlob, S. Cramm, K. Veltruská, V. Matolín, S. Nemšák and C. M. Schneider, *Surf. Sci.* 2018, **671**, 1–5.
46 F. A. Kröger and H. J. Vink, *Solid State Phys.* 1956, **3**, 306–435.
47 Z. A. Feng, F. El Gabaly, X. Ye, Z.-X. Shen and W. C. Chueh, *Nat. Commun.* 2014, **5,** 4374.
48 M. Capdevila-Cortada and N. López, *Nature Mater.* 2017, **16**, 328–334.
49 J. Höcker, J.-O. Krisponeit, T. Schmidt, J. Falta and J. I. Flege, *Nanoscale* 2017, **9**, 9352–9358.
50 T. X. T. Sayle, F. Caddeo, X. Zhang, T. Sakthivel, S. Das, S. Seal, S. Ptasinska and D. C. Sayle, *Chem. Mater.* 2016, **28**, 7287–7295.
51 Z. Zhao, M. Uddi, N. Tsvetkov, B. Yildiz and A. F. Ghoniem, *J. Phys. Chem. C* 2016, **120**, 16271–16289.
52 N. Knoblauch, L. Dörrer, P. Fielitz, M. Schmücker and G. Borchardt, *Phys. Chem. Chem. Phys.* 2015, **17**, 5849–5860.
53 H. A. Al-Madfaa and M. M. Khader, *Mater. Chem. Phys.* 2004, **86**, 180–188.
54 W. C. Chueh, A. H. McDaniel, M. E. Grass, Y. Hao, N. Jabeen, Z. Liu, S. M. Haile, K. F. McCarty, H. Bluhm and F. E. Gabaly, *Chem. Mater.* 2012, **24**, 1876–1882.
55 G. E. Murgida and M. V. Ganduglia-Pirovano, *Phys. Rev. Lett.* 2013, **110**, 246101.
56 S. Torbrügge, M. Reichling, A. Ishiyama, S. Morita and Ó. Custance, *Phys. Rev. Lett.* 2007, **99**, 56101.
57 M. Capdevila-Cortada and N. López, *Nat. Mater* 2017, **16**, 328–334.
58 D. Zhang, Z.-K. Han, G. E. Murgida, M. V. Ganduglia-Pirovano and Y. Gao, *Phys. Rev. Lett.* 2019, **122**, 096101.

Establishing Structure-Sensitivity of Ceria Reducibility: Real Time Observations of Surface-Hydrogen Interactions

Tomáš Duchoň[1,2,*], Johanna Hackl[1], David N. Mueller[1,*], Jolla Kullgren[3], Dou Du[3], Sanjaya D. Senanayake[4], Caroline Mouls[5], Daniel M. Gottlob[1], Muhammad I. Khan[1], Stefan Cramm[1], Kateřina Veltruská[2], Vladimír Matolín[2], Slavomír Nemšák[1,6,*], Claus M. Schneider[1,7].

[1]*Peter-Grünberg-Institut 6, Forschungszentrum Jülich, 52425 Jülich, Germany*

[2]*Department of Surface and Plasma Science, Faculty of Mathematics and Physics, Charles University, 18000 Prague, Czech Republic*

[3]*Department of Chemistry−Ångström Laboratory, Uppsala University, Box 538, S-751 21 Uppsala, Sweden*

[4]*Department of Chemistry, Brookhaven National Laboratory, Upton, New York 11973, USA*

[5]*Laboratório Nacional de Luz Síncrotron, 13083 Campinas - SP, Brazil*

[6]*Advanced Light Source, Lawrence Berkeley National Laboratory, Berkeley, CA, USA*

[7]*Department of Physics, University of California, Davis, CA, USA*

Details of the preparation process: Figure S1 shows LEEM images of the preparation process. The clean Cu (111) single-crystal was annealed at 870 K in an atmosphere of 5×10^{-7} mbar of oxygen partial pressure right before cerium deposition, which helped to further decrease the amount of carbon impurities on the surface and to establish a well-defined surface oxygen chemical potential. No visible defects or imperfections are present in the observed region of the substrate, although other parts of the single-crystal might be affected by such structures.[1] The mean terrace width of the prepared substrate is of the order of tens to hundreds of nm (Figure S1(a)), indicating very flat and well-defined growth support.

The ceria growth is done by evaporation of cerium metal in the same oxygen ambience. Immediately after the beginning of the cerium deposition, the nucleation of ceria islands starts, and several structures are formed within the observed field of view (Figure S1(b)), with their nucleation sites pinned to the substrate's step boundaries. As the growth process continues, the step boundaries bend to accommodate the presence of the growing ceria islands (Figure S1(c)).

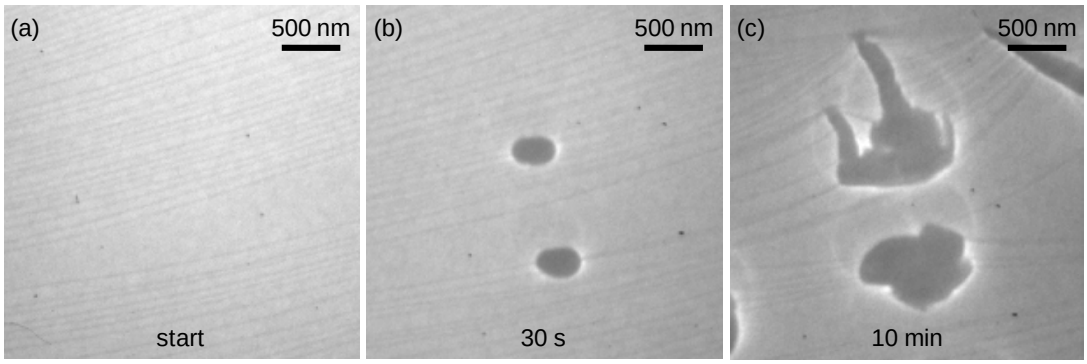

Figure S1. LEEM images (recorded at 1 eV) during growth of ceria islands on Cu (111) substrate in 5×10^{-7} mbar O_2 at 720 K: (a) clean substrate, (b) after 30 s, (c) after 10 min of growth.

The different surface orientations of islands can be distinguished by intensity-voltage LEEM.[2] Depending on the electron beam energy with respect to the sample potential (also called start energy), the two surface orientations show different intensities as a result of their different low-energy electron reflectivities.[3] Using a LEEM start energy of 9 eV in Figure 1(b), the (111) islands appear brighter than the (100) ones. The ultimate confirmation, however, comes from the μ-LEED measurements.

Determination of CeO_x island thickness: Figure S2 shows Cu L3 XAS spectra extracted from the exposed substrate and from below the grown islands that were used for the islands' thickness determination.

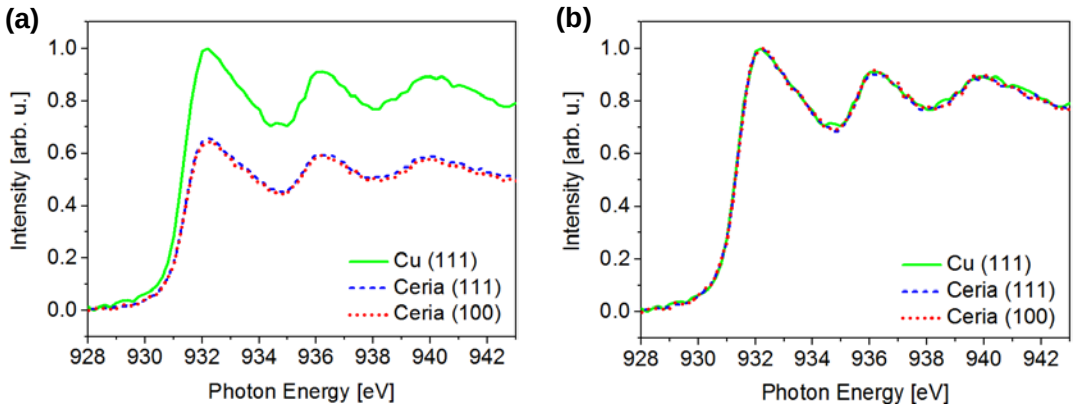

Figure S2. Cu L_3 edge X-ray absorption spectra extracted at three different locations on the sample: (a) with subtracted pre-edge; (b) normalized to the same step-edge difference showing the overlap of the spectral shapes, which rules out the difference in Cu chemical state on the surface and under the islands.

Stoichiometry in X-PEEM: The difference in ceria reduction can be seen in the X-PEEM images of the islands taken at the photon energy corresponding to the Ce^{4+} peak (883.4 eV). In Figure S3 (a) the islands are shown in their uniform oxidation state after the growth and in Figure S3 (b) they are shown after 18 h in hydrogen. The sole (111) island in Figure S3 (b) is visibly brighter than all the other islands, which reveals its higher Ce^{4+} content.

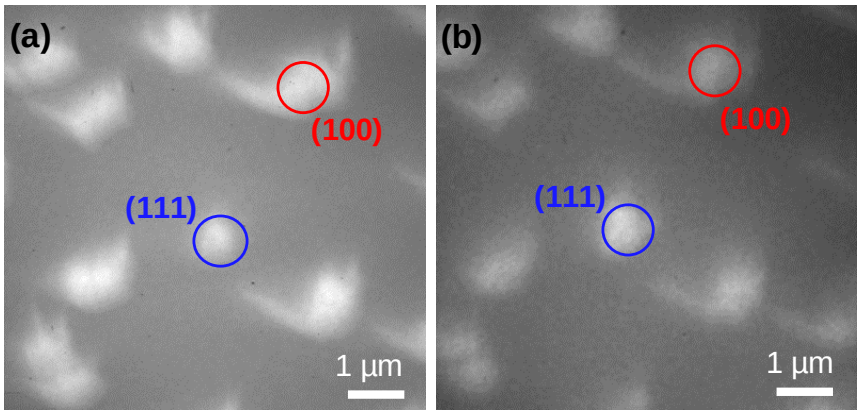

Figure S3. X-PEEM images at Ce M_5 edge (hν=883.4 eV) of the CeO_2 (111) and (100) islands in Figure 2(a): (a) after growth, measured in 5×10^{-7} mbar O_2 at 700K; (b) after 18 h in 1.5×10^{-6} mbar H_2 at 700K.

Details on theoretical calculations: Initial theoretical calculations were based on density functional theory (DFT) in the implementation with plane waves and pseudopotentials using the generalized gradient corrections to the local density functional approximations as proposed by Perdew et al. (PBE).[4] In addition, we employ a Hubbard correction (+U) according to the method proposed by Dudarev et al. to accurately treat the strongly correlated f -electrons in Ce .[5] Our simulations include non-spherical contributions from the gradient corrections inside the PAW spheres using the flag LASPH = .TRUE. in the VASP input. All calculations have been made with a U-value of 5 eV which has been shown to give a good description of stoichiometric and reduced ceria in previous studies.[6,7,8,9] Results in table S1 show oxygen vacancy

formation energies as a function of the different level of ceria reduction for the two respective surface terminations of 3ML thick slabs.

(111)		(100)	
E_{vac} [eV]	C(Ce^{4+})	E_{vac} [eV]	C(Ce^{4+})
1.330	0.958	0.650	0.917
1.540	0.833		
2.060	0.667	1.380	0.667
2.230	0.333	2.230	0.333

Table S1. Calculated oxygen vacancy formation energies E_{vac} for different ceria stoichiometry (shown as Ce^{4+} concentrations) and surface termination using DFT+U.

Another approach in theoretical simulations was based on DFT in the implementation with plane waves and pseudopotentials using the Hybrid density functional proposed by Heyd-Scuseria-Ernzerhof (HSE06).[10,11] Table S2 shows the calculated oxygen vacancy formation energies for the different Ce^{4+} concentrations in a three ML slabs of ceria (111) and (100).

(111)		(100)	
E_{vac} [eV]	C(Ce^{4+})	E_{vac} [eV]	C(Ce^{4+})
2.382	0.958		
2.383	0.917	1.611	0.917
2.771	0.833		
3.332	0.667	2.538	0.667
3.419	0.333	3.175	0.333

Table S2. Calculated oxygen vacancy formation energies E_{vac} for different ceria stoichiometry (shown as Ce^{4+} concentrations) and surface termination using hybrid density functionals.

[1] Duchoň, T., Hackl, J., Höcker, J., Veltruská, K., Matolín, V., Falta, J., Cramm, S., Nemšák, S., Schneider, C. M., Flege, J. I. & Senanayake, S. D. Exploiting micro-scale structural and chemical observations in real time for understanding chemical conversion: LEEM/PEEM studies over CeO_x-Cu(111). *Ultramicroscopy* **183**, 84–88 (2017).

[2] Flege, J. I. & Krasovskii, E. E. Intensity–voltage low-energy electron microscopy for functional materials characterization. *Phys. Status Solidi RRL* **8**, 463–477 (2014).

[3] Flege, J. I., Kaemena, B., Meyer, A., Falta, J., Senanayake, S. D., Sadowski, J. T., Eithiraj, R. D. & Krasovskii, E. E. Origin of chemical contrast in low-energy electron reflectivity of correlated multivalent oxides: The case of ceria. *Phys. Rev. B* **88**, 235428 (2013).

[4] Perdew, J. P., Burke, K. & Ernzerhof, M. Generalized Gradient Approximation Made Simple. *Phys. Rev. Lett.* **77**, 3865−3868 (1996).

[5] Dudarev, S. L., Botton, G. A., Savrasov, S. Y., Humphreys, C. J. & Sutton, A. P. Electron-Energy-Loss Spectra and the Structural Stability of Nickel Oxide: An LSDA+U Study. *Phys. Rev. B* **57**, 1505−1509 (1998).

[6] Andersson, D. A., Simak, S. I., Johansson, B., Abrikosov, I. A. & Skorodumova, N. V. Modeling of CeO2, Ce2O3, and CeO2-x in the LDA+U Formalism. *Phys. Rev. B* **75**, 035109 (2007).
[7] Castleton, C. W. M., Kullgren, J. & Hermansson, K. Tuning LDA + U for Electron Localization and Structure at Oxygen Vacancies in ceria. *J. Chem. Phys.* **127**, 244704 (2007).
[8] Loschen, C., Carrasco, J., Neyman, K. M. & Illas, F. First Principles LDA+U and GGA+U Study of Cerium Oxides: Dependence on the Effective U Parameter. *Phys. Rev. B* **75**, 035115 (2007).
[9] Jiang, Y., Adams, J. B. & van Schilfgaarde, M. Density-functional Calculation of CeO_2 Surfaces and Prediction of Effects of Oxygen Partial Pressure and Temperature on Stabilities. *J. Chem. Phys.* **123**, 064701 2005).
[10] Heyd, J., Scuseria, G.E. &. Ernzerhof, M. *Journal of Chemical Physics* **118**, 8207 (2003).
[11] Heyd, J., Scuseria, G. E. & Ernzerhof, M. *The Journal of Chemical Physics* **124**, 219906 (2006).